

Challenging the Weak Cosmic Censorship with Phantom Fields

Giovanni Caridi,^{1,2} Fabrizio Corelli,^{3,1,2} and Paolo Pani^{1,2}

¹*Dipartimento di Fisica, Sapienza Università di Roma, Piazzale Aldo Moro 5, 00185, Roma, Italy*

²*INFN, Sezione di Roma, Piazzale Aldo Moro 2, 00185, Roma, Italy*

³*Max Planck Institute for Gravitational Physics (Albert Einstein Institute), Am Mühlenberg 1, 14476 Potsdam, Germany*

Penrose’s weak cosmic censorship conjecture asserts that spacetime singularities produced by gravitational collapse are generically hidden behind event horizons, thus preventing them from causally influencing distant observers and preserving the predictability of the exterior region. In this work, we probe this conjecture in a setup that deliberately violates one of its central assumptions – the dominant energy condition – by considering the spherical collapse of a *phantom* scalar field with negative energy density. In principle, such a field could produce a Schwarzschild geometry with *negative* mass and therefore no event horizon. Our aim is to assess whether, once the dominant energy condition is abandoned, the fully coupled evolution of matter and geometry can dynamically generate or expose naked singularities, thereby probing the robustness of cosmic censorship. To this end, we perform high-accuracy numerical relativity simulations based on fourth-order finite-difference schemes. Starting from smooth, asymptotically flat initial data representing regular phantom scalar wave packets, we follow their fully nonlinear evolution through collapse or dispersion. While an ordinary (positive-energy) scalar field exhibits the standard Choptuik critical behavior at the threshold of black-hole formation, the phantom field displays qualitatively different dynamics. For all amplitudes considered, we find no evidence for trapped surfaces, naked singularities, or alternative stationary end states. Instead, the phantom scalar field always disperses, suggesting that cosmic censorship remains dynamically preserved even in the presence of negative-energy matter.

I. INTRODUCTION

The notion of a *singularity* in General Relativity represents one of the most subtle and conceptually challenging aspects of the theory. As emphasized by Geroch [1], the familiar intuition of a singular point originates from classical field theories formulated on a fixed background spacetime, where certain physical quantities diverge while the geometric arena remains well defined. In classical electrodynamics, for instance, the electric field of a point charge diverges at the source, yet the background spacetime itself remains unaffected. In General Relativity, however, this picture breaks down: the metric is itself a dynamical field, and there is no external geometric structure relative to which singular behavior can be defined. In the absence of a fixed background, the very meaning of singularity becomes more subtle and less intuitive.

For this reason, no universally accepted definition of singularity exists in General Relativity. Historically, two main characterizations have been employed. One identifies singularities with the divergence of curvature invariants, such as the Kretschmann scalar [2]. The other, more geometrically robust, definition characterizes a spacetime as singular if it is *geodesically incomplete* [3]. In the formulation adopted by Wald [4] (see also [5–9]), a spacetime is singular if it contains at least one timelike or null geodesic that cannot be extended to arbitrary values of its affine parameter. Physically, this corresponds to a freely falling observer (or photon) whose worldline ends after a finite proper time (or affine parameter), signaling a breakdown of predictability. Even this definition, however, is not entirely free from ambiguities, as it may depend on the differentiable structure or on possible ex-

tensions of the spacetime [1].

A decisive step forward was made by Penrose [9], who demonstrated that singularities are not artifacts of symmetry but arise generically under gravitational collapse. When a sufficiently massive body can no longer support itself against its own gravity, collapse leads inevitably to geodesic incompleteness. This insight culminated in the singularity theorems of Hawking and Penrose [6], which show that, under suitable energy and causality conditions, singularities are unavoidable in broad classes of physically relevant spacetimes, including cosmological models and collapsing configurations.

The existence of singularities, however, raises a profound issue. In principle, a singularity formed during collapse need not be hidden behind an event horizon. If visible to distant observers (i.e., if *naked*), such singularities would signal a breakdown of determinism, since classical evolution would cease to be predictable beyond their formation. Some solutions of Einstein’s equations (e.g. certain extremal configurations, dynamical instabilities, and collapse of exotic matter) have been shown to admit naked singularities under specific conditions [10–15].

To address this threat to predictability, Penrose formulated the *weak cosmic censorship conjecture* [16], which asserts that singularities arising from the gravitational collapse of physically reasonable matter – obeying the dominant energy condition and evolving from regular initial data – are generically hidden within event horizons. Despite decades of effort, this conjecture remains unproven in full generality. A variety of partial results support its validity in restricted settings [17–20]. Counterexamples are known in higher dimensions [21, 22], or for test particles [19, 23, 24] only when neglecting back-

reaction [19, 25, 26].

Scalar-field collapse has played a central role in this debate. Christodoulou’s analytical studies demonstrated that spherically symmetric self-gravitating scalar fields can lead either to black-hole formation or, for finely tuned initial data, to the development of naked singularities [18, 27]. Although such naked solutions are unstable under generic perturbations, these results highlight the delicate boundary between collapse outcomes.

Numerical relativity simulations [28] enabled fully nonlinear investigations of collapse, beginning with Choptuik’s discovery of critical phenomena [29]. Subsequent studies extended these analyses to massive, complex, charged, and self-interacting scalar fields, as well as to perfect fluids [30–34].

In this work, we deliberately relax one of the key assumptions underlying the weak cosmic censorship conjecture, namely the dominant energy condition. We consider a *phantom* scalar field, described by an inverted-sign kinetic term and therefore characterized by negative energy density. Such fields violate the standard energy conditions [6] in a controlled manner and provide a useful theoretical laboratory to probe the robustness of horizon formation. Indeed, a collapsing phantom field in flat spacetime might in principle form a Schwarzschild metric with *negative* mass, which does not feature an event horizon and exposes a naked singularity.

Here we focus on a minimal and clean setup: the spherical collapse of a massless phantom scalar field in asymptotically flat spacetime. Unlike canonical scalar collapse, where attractive gravity competes with dispersion and leads to well-known critical behavior, the inverted kinetic term induces an effectively repulsive gravitational response. This raises a natural question: can such a violation of the dominant energy condition prevent horizon formation while still allowing singular structures to develop, thereby challenging the weak cosmic censorship conjecture?

To answer this question, we perform high-accuracy numerical relativity simulations of smooth, localized wave packets, systematically varying their amplitude and width. Rather than searching for critical scaling laws, our primary goal is to characterize qualitatively the possible dynamical regimes: dispersion, bounce, horizon or other regular end-state formation, or the emergence of naked singularities or other exotic solutions. This setup provides a fully nonlinear and controlled framework to investigate how violations of the energy conditions affect gravitational collapse and to assess the robustness of cosmic censorship beyond its standard assumptions.

Despite being conceptually simple, this setup has received little attention in the literature and, to the best of our knowledge, has only been considered in [35, 36]. In that work, the collapse of scalar fields was studied within an Einstein-Maxwell-dilaton model allowing for phantom fields. Among the configurations analyzed, the case involving only a phantom dilaton coupled to gravity was mentioned to evolve toward a regular spacetime with the

scalar field dispersing at infinity.

In this work we revisit and extend this scenario by systematically exploring the parameter space of the initial wave packet. Our goal is to characterize the dynamics more broadly, investigate the possible formation of naked singularities or other exotic outcomes, and assess the robustness of the behavior previously reported in [35, 36].

The remainder of this manuscript is organized as follows. In Sec. II we present the theoretical framework and numerical implementation. In Sec. III we discuss the collapse of a canonical scalar field, serving as a benchmark. In Sec. IV we analyze the phantom case and characterize the resulting spacetime dynamics. Our conclusions are summarized in Sec. V. Appendix A reports convergence tests of the numerical code.

II. NUMERICAL SETUP

Our code simulates the spherical collapse of wave packets of a scalar field in an initially flat background using Schwarzschild-like coordinates. We start this section by introducing the model and the system of equations we integrate numerically, and then describe the implementation of our code. Here and in the rest of the paper we adopt geometrized units, setting $G = c = 1$. We express all dimensional quantities in units of an arbitrary mass scale \tilde{M} .

A. Evolution equations and constraints

We consider the spherically symmetric Einstein-Klein-Gordon system for a real scalar field ξ . The action is

$$S = \frac{1}{16\pi} \int_{\Omega} \sqrt{-g} \left[R + C(\nabla_{\mu}\xi)(\nabla^{\mu}\xi) \right] d^4x, \quad (1)$$

where R is the Ricci scalar, ξ is the scalar field, $g_{\mu\nu}$ is the spacetime metric, and $C \in \{+1, -1\}$ determines the sign of the kinetic term: $C = +1$ for a phantom field, and $C = -1$ for a canonical scalar field. Varying (1) with respect to $g_{\mu\nu}$ and ξ we obtain the field equations

$$G_{\mu\nu} = R_{\mu\nu} - \frac{1}{2}g_{\mu\nu}R = T_{\mu\nu}, \quad (2)$$

$$\square\xi = 0, \quad (3)$$

where $\square = \nabla_{\mu}\nabla^{\mu}$ and the stress-energy tensor contains only the contribution of the scalar field:

$$T_{\mu\nu} = C(-2(\nabla_{\mu}\xi)(\nabla_{\nu}\xi) + g_{\mu\nu}\nabla_{\rho}\xi\nabla^{\rho}\xi). \quad (4)$$

We express the line element using Schwarzschild-like coordinates:

$$ds^2 = -e^{2\alpha(t,r)} dt^2 + e^{2\beta(t,r)} dr^2 + r^2 d\Omega_2^2, \quad (5)$$

where $\alpha(t, r)$ and $\beta(t, r)$ are metric functions that depend only on coordinate time and areal radius. While

this choice makes the numerical implementation simple, it produces a coordinate singularity at the horizon when a black hole forms. To handle this, we halt the evolution upon horizon detection by introducing diagnostic thresholds on g_{tt} and on quasi-local quantities.

For the scalar field, we introduce the auxiliary variables

$$\Theta = \partial_r \xi, \quad (6)$$

$$\Pi = n^\mu \nabla_\mu \xi = e^{-\alpha} \partial_t \xi, \quad (7)$$

where Π is the conjugate momentum of ξ and $n^\mu = (e^{-\alpha}, 0, 0, 0)$ is the 4-velocity of the Eulerian observer.

In terms of Π and Θ , the equations of motion can be rewritten as a system of partial differential equations suitable for the numerical evolution:

$$\partial_t \xi = e^\alpha \Pi, \quad (8)$$

$$\partial_t \Theta = e^\alpha \partial_r \alpha \Pi + e^\alpha \partial_r \Pi, \quad (9)$$

$$\partial_t \Pi = \frac{e^\alpha (e^{-2\beta} (r \partial_r \Theta + \Theta) + \Theta (Cr^2 \Pi^2 + 1))}{r}, \quad (10)$$

$$\partial_t \beta = -C r e^\alpha \Theta \Pi, \quad (11)$$

$$\partial_r \beta = -\frac{e^{2\beta} (Cr^2 \Pi^2 + 1) + Cr^2 \Theta^2 - 1}{2r}, \quad (12)$$

$$\partial_r \alpha = \frac{e^{2\beta} (1 - Cr^2 \Pi^2) - Cr^2 \Theta^2 - 1}{2r}, \quad (13)$$

The first four relations correspond to the evolution equations for the dynamical variables, while the last two represent the constraint equations that must be satisfied at each time step to ensure the consistency of the system.

In the absence of a scalar field ($\xi = 0$), β is stationary and one obtains exactly the Schwarzschild metric

$$e^{2\alpha} = e^{-2\beta} = 1 - \frac{2M}{r}. \quad (14)$$

B. Numerical integration

The numerical integration of Eqs. (8)–(11) is performed using the method of lines [37]: the evolution equations are integrated in time at each grid point, while the spatial derivatives on the right-hand sides are evaluated by finite differences. Specifically, we employ the fourth order accurate Runge-Kutta method for time integration, and the fourth order accurate centered finite differences formula for the spatial derivatives.

We use a uniform numerical grid, staggered by half a grid step in order to avoid placing a grid point on the origin, where the right-hand sides of Eqs. (10), (12) and (13) cannot be evaluated numerically. In other words, the grid points are located at

$$r_j = (j + \frac{1}{2}) \Delta r, \quad j = 0, \dots, N_p - 1, \quad (15)$$

where Δr is the grid spacing and N_p the number of grid points.

To apply centered stencils at the first nodes we introduce three ghost zones on the left, at $r_{-1} = -\Delta r/2$, $r_{-2} = -3\Delta r/2$, and $r_{-3} = -5\Delta r/2$: in these cells the variables are not evolved, but at each time step they are filled by enforcing regularity and spherical symmetry. In particular, for the scalars α , β , ξ and Π we impose even parity, whereas for $\Theta = \partial_r \xi$ we impose odd parity. At the outer boundary r_∞ , we add three ghost zones beyond the last physical grid point, whose values remain frozen after initialization. This is legitimate because the initial profile of ξ is localized close to the center of the spatial domain and rapidly decays toward the outer boundary. Moreover, we choose a combination of the size of the grid and the total time of integration that prevent signals from reaching it. The scalar field characteristics have speeds [38]

$$v_\pm = \frac{dr}{dt} = \pm e^{\alpha-\beta}, \quad (16)$$

which tend to 1 as $r \rightarrow \infty$, since $\alpha, \beta \rightarrow 0$. Consequently, as long as $t/r_\infty \lesssim 1$, no signal reaches the outer boundary, and the fields there remain constant.

To set the time integration step Δt , it is convenient to introduce the Courant-Friedrichs-Lewy (CFL) factor

$$\overline{\text{CFL}} = v_{\text{char}} \frac{\Delta t}{\Delta r}, \quad (17)$$

where $v_{\text{char}} = |v_\pm|$ denotes the propagation speed of signals within the system. Stability of the simulation requires the CFL factor above to be smaller than an upper value which depends on the integration scheme. For the simulations performed in this work, we first choose a fiducial value of the CFL factor, and then set the time step as

$$\Delta t = \text{CFL} \Delta r. \quad (18)$$

The factor CFL corresponds to $\overline{\text{CFL}}$ in Eq. (17) when $v_{\text{char}} \approx 1$. This approximation works well in cases where the spacetime is nearly flat, and the scalar field assumes only small values. However, we will see that in our simulations v_{char} can become significantly larger than unity when the initial scalar wave packet has a large amplitude, which requires choosing a sufficiently small value of CFL.

For each time step, the profile of the metric function α is obtained by integrating the constraint (13) along the radial direction. In particular, since Eq. (13) has the form

$$\partial_r \alpha = F[r, \beta, \Theta, \Pi], \quad (19)$$

we can obtain the profile of α by integrating the right-hand side as

$$\alpha(r) = \alpha(r_{\infty+2}) + \int_{r_{\infty+2}}^r F dr, \quad (20)$$

where $r_{\infty+2}$ is the second ghost zone at the outer boundary. The integral is evaluated with the Simpson's rule,

and starting from $r_{\infty+2}$ (where the values of the fields are given by our boundary conditions) allows us to reach fourth order convergence on the last grid point r_{∞} .

To ensure the stability of the evolution and suppress numerical instabilities arising from high-frequency modes, we introduce a fifth-order Kreiss-Oliger dissipation term [39, 40], defined as

$$\partial_t u \rightarrow \partial_t u - \frac{\eta_{\text{KO}}}{64\Delta t} (\Delta r)^6 (D_+^3 D_-^3 u), \quad (21)$$

where u denotes a generic field, η_{KO} is a coefficient to be fixed below, while D_{\pm} are first-order finite difference operators with one-sided backward ($-$) and forward ($+$) schemes. The computation of this correction requires the use of three grid points on each side of the point where it is evaluated; the use of three ghost zones allows us to perform this computation even at the boundaries.

C. Initial data

As initial data of the scalar field we considered both a Gaussian and a tanh-type profile

$$\xi(t=0, r)_{\text{Gaussian}} = \frac{A}{r} \exp\left[-\frac{(r-r_0)^2}{2\sigma^2}\right], \quad (22)$$

$$\xi(t=0, r)_{\text{tanh}} = \frac{A}{2} \left[\tanh\left(\frac{r-\hat{r}_1}{\sigma}\right) - \tanh\left(\frac{r-\hat{r}_2}{\sigma}\right) \right]. \quad (23)$$

In Eq. (22), A denotes the field amplitude, r_0 the initial central position of the pulse, and σ its characteristic width. In Eq. (23), the parameters \hat{r}_1 and \hat{r}_2 define the left and right edges of the tanh-like profile, respectively, and thus determine the radial interval over which the function $\xi(r)$ attains a value close to the plateau A . More precisely, for $r \lesssim \hat{r}_1$ and $r \gtrsim \hat{r}_2$ the function rapidly approaches zero, whereas in the intermediate region $\hat{r}_1 \lesssim r \lesssim \hat{r}_2$ it remains approximately constant (see Fig. 1 for a schematic representation). The separation $\hat{r}_2 - \hat{r}_1$ therefore sets the effective width of the smoothed step, while the parameter σ controls the sharpness of the transition between the near-vanishing regions and the central plateau.

After setting the profile of ξ , the auxiliary fields Θ and Π are initialized as

$$\Theta(t=0, r) = \partial_r \xi(t=0, r), \quad (24)$$

$$\Pi(t=0, r) = \xi(t=0, r)/r + \Theta(t=0, r). \quad (25)$$

The choice in Eq. (25) ensures that the initial wave is predominantly ingoing. The initial data are chosen so that the main part of the wave packet is initially concentrated near the inner boundary. The profiles of the metric functions $\alpha(t=0, r)$ and $\beta(t=0, r)$ are obtained by integrating numerically the constraints (13) and (12) starting from the first grid point $r_1 = \Delta r/2$ and moving outward. In order to obtain the initial values for the

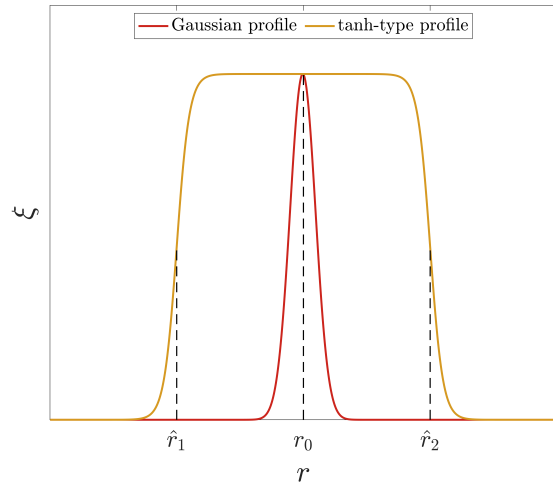


Figure 1. Representative initial profiles of the scalar field $\xi(r)$ used in the numerical simulations. The Gaussian profile (red curve) corresponds to a localized pulse, while the tanh-type profile (yellow curve) produces a smoothed step with an approximately constant plateau.

integration procedure, we perform a Taylor expansion of the metric function at the origin

$$\alpha(t, r) = \alpha_0(t) + \alpha_2(t) r^2 + \mathcal{O}(r^4), \quad (26)$$

$$\beta(t, r) = \beta_0(t) + \beta_2(t) r^2 + \mathcal{O}(r^4), \quad (27)$$

in which terms of odd power in r vanish, consistently with parity. Regularity of the metric at $r=0$ requires that $e^{2\beta(t,0)} = 1$, and hence $\beta_0 = 0$. α_0 is instead a free parameter as, due to our choice of the metric ansatz (5), a shift of the profile of α can be compensated with a rescaling of the coordinate time. We therefore decide to initially set $\alpha_0 = 0$. Substituting the expansions (26) and (27) in the constraint equations we can compute α_2 and β_2 . The values of the metric functions at the first grid point r_1 then read

$$\alpha(t=0, r_1) = -\frac{C}{3} \Pi^2(r_1) r_1^2, \quad (28)$$

$$\beta(t=0, r_1) = -\frac{C}{6} \Pi^2(r_1) r_1^2. \quad (29)$$

After performing the numerical integration of Eqs. (13) and (12) with the fourth order accurate Runge-Kutta method up to the outer boundary, we shifted the profile of $\alpha(t=0, r)$ in order to impose

$$\alpha(r_{\infty}) = 0, \quad (30)$$

which corresponds to requiring that the coordinate time t coincides with the proper time at spatial infinity.

In Fig. 2 we show, as an example, the initial profiles of e^{α} , e^{β} and v_{char} corresponding to a Gaussian wave packet centered in $r_0 = 10\bar{M}$, having initial amplitude $A = 0.1\bar{M}$ and width $\sigma = \bar{M}$. As we can see the metric

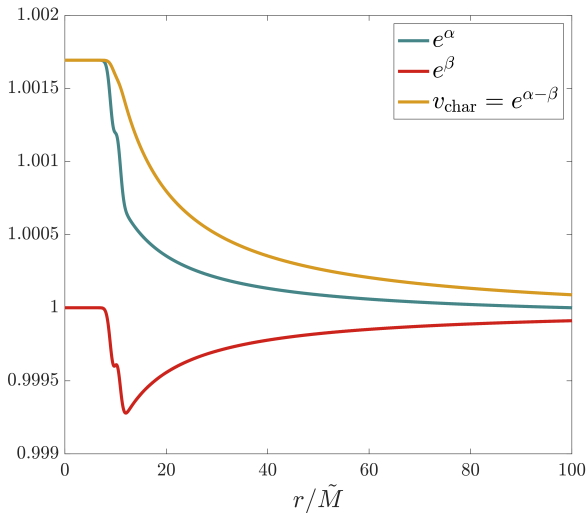


Figure 2. Initial profiles for e^α , e^β and v_{char} , describing a nearly flat spacetime locally perturbed by a Gaussian pulse of the phantom field centered at $r_0 = 10\tilde{M}$. The amplitude of the wave packet is $A = 0.1\tilde{M}$ and its width is $\sigma = \tilde{M}$.

is essentially flat for values of r far from the wave position and inside it, while around $r \approx 10\tilde{M}$ both e^α and e^β decrease due to the presence of the Gaussian pulse. After that, the metric functions start approaching unity, consistently with asymptotic flatness.

D. Diagnostic variables

To investigate the numerical evolution of the phantom-field collapse, we introduce a set of diagnostic quantities to monitor the geometric and physical properties of the spacetime. Among these, a central role is played by the Kretschmann scalar, which provides a coordinate-invariant measure of the spacetime curvature [2]. It is defined as

$$K = R_{\mu\nu\rho\sigma}R^{\mu\nu\rho\sigma} = \frac{8Cr^2e^{-4\beta}}{r^4} (\Theta^2 - e^{2\beta}\Pi^2) \times (-e^{2\beta}(Cr^2\Pi^2 + 1) + Cr^2\Theta^2 + 1) + \frac{12e^{-4\beta}}{r^4} (e^{2\beta} - 1)^2. \quad (31)$$

where $R_{\mu\nu\rho\sigma}$ is the Riemann tensor. The above expression was obtained by explicitly computing the Riemann tensor $R_{\mu\nu\rho\sigma}$ from the line element (5) and subsequently using the evolution system (8)-(13) to express the result in terms only of the dynamical variables. Inspecting the spacetime behavior of K enables us to assess whether singularities develop during the simulations. In particular, we monitor whether K remains finite and regular throughout the evolution or exhibits divergent behavior in localized regions, which would signal the formation of curvature singularities.

Alongside the Kretschmann scalar, we monitor the Misner-Sharp mass [41], which in our coordinates takes the form

$$M_{\text{MS}}(t, r) = \frac{r}{2} (1 - g^{\mu\nu} \partial_\mu r \partial_\nu r) = \frac{r}{2} (1 - e^{-2\beta(t, r)}). \quad (32)$$

This quantity provides a quasi-local measure of the gravitational mass contained within a sphere of areal radius r . In spherical symmetry, it also serves as a convenient diagnostic for the formation of apparent horizons. Indeed, trapped surfaces are characterized by the condition

$$\frac{2M_{\text{MS}}(t, r)}{r} \geq 1, \quad (33)$$

which signals the vanishing of the expansion of future directed outgoing null geodesics.

In the phantom-field case, however, the effective energy density can be negative, contributing negatively to the mass function. One therefore expects that Eq. (33) is not satisfied, thereby preventing the formation of trapped regions.

In the case of a canonical scalar field ($C = -1$), one instead expects the formation of an apparent horizon, provided the amplitude of the initial wave packet is sufficiently large. However, within the metric ansatz in Eq. (5), the coordinates are not horizon-penetrating. As a result, black-hole formation cannot be reliably identified solely by tracking the regions where condition (33) is satisfied, since coordinate effects may obscure the approach to horizon formation.

Following Ref. [38], we therefore monitor the characteristic speeds of the system, which encode information about its causal structure. In particular, apparent horizons can be identified as the locations where the characteristic speed of outgoing radial null rays, v_+ , vanishes. Physically, this corresponds to the point where outward-propagating light fronts become momentarily frozen, signaling the onset of a trapped region. Operationally, we define the apparent horizon radius as the outermost spherical shell where v_+ drops below a prescribed threshold ε [38, 42]:

$$r_{\text{AH}} = \max \{ r \mid v_+ = \exp(\alpha(t, r) - \beta(t, r)) < \varepsilon \}. \quad (34)$$

We will typically take $\varepsilon = 10^{-6}$ as a fiducial value.

The combined use of the Kretschmann scalar and this horizon-finding criterion allows us to characterize the end state of the spherical collapse, distinguishing between dispersion, black-hole formation, and potential violations of cosmic censorship or the emergence of alternative stationary configurations.

III. COLLAPSE OF WAVE PACKETS OF A CANONICAL SCALAR FIELD

In order to validate our numerical implementation, in addition to the convergence analysis reported in Appendix A, we simulated the gravitational collapse of a

canonical scalar field and verified that we recover the key features of Choptuik’s seminal results [29]. In particular, we checked for the existence of a critical amplitude A^* , independent of numerical parameters, that marks the threshold between dispersion and black-hole formation.

To this end, we set $C = -1$ and considered Gaussian initial data with fixed parameters $\sigma = \tilde{M}$ and $r_0 = 10\tilde{M}$, varying only the amplitude A of the scalar field.

For sufficiently small amplitudes, the scalar field disperses, leaving behind a regular spacetime. An illustrative example is shown in the left panels of Fig. 3, corresponding to $A = 0.2\tilde{M}$. Each panel displays a different time snapshot of the evolution. The red solid curve represents the scalar-field profile, while the yellow dashed curve shows the outgoing characteristic velocity v_+ . The wave packet initially propagates inward ($t \lesssim 10\tilde{M}$), reaches the central region, and subsequently disperses ($t \gtrsim 10\tilde{M}$). Throughout the evolution, the characteristic velocity remains close to unity and never approaches zero, indicating that no trapped region forms.

For larger initial amplitudes, the evolution instead leads to black-hole formation. This behavior is illustrated in the right panels of Fig. 3, which show the case $A = \tilde{M}$ using the same conventions as in the left panels. As time progresses, the outgoing characteristic velocity v_+ decreases and eventually approaches zero within a finite radial interval. In this region, the evolution effectively freezes, reflecting the fact that outgoing light rays can no longer propagate to larger radii. This signals the formation of a trapped region, which we identify as an apparent horizon.

Using the criterion of Eq. (34), we estimate the apparent-horizon radius to be $r_{\text{AH}} = 1.653\tilde{M}$. At the time of formation, the Misner-Sharp mass extracted at the outermost point of the physical grid is $M_{\text{MS}} = 0.849\tilde{M}$, in good agreement with the Schwarzschild relation $r_{\text{H}} = 2M$. The small deviation from exact equality is expected, since the initial data are not purely ingoing and residual scalar-field energy remains outside the horizon. These results provide clear numerical evidence of black-hole formation within the chosen configuration.

Following Choptuik’s analysis, we systematically varied the amplitude A while keeping σ and r_0 fixed, and identified the critical value A^* separating dispersive evolutions from black-hole formation. To ensure robustness, this study was repeated at different spatial resolutions and CFL factors.

The results are shown in Fig. 4, where we plot the critical amplitude A^* as a function of the CFL factor, with different colors corresponding to different spatial resolutions (labeled by the number of grid points N_p). As the resolution increases or the CFL factor decreases, the critical amplitude converges toward

$$A^* \simeq 0.566\tilde{M}.$$

The stabilization of A^* at high resolution confirms that the code reliably captures the threshold between disper-

sion and collapse, and reproduces the expected critical behavior of canonical scalar-field collapse.

IV. COLLAPSE OF WAVE PACKETS OF A PHANTOM SCALAR FIELD

We now turn to the case of a phantom scalar field, corresponding to $C = +1$. We observe that for sufficiently small amplitudes the wave packet disperses, similarly to the canonical case ($C = -1$). However, for larger values of the amplitude A , the numerical evolution eventually breaks down. While this behavior could in principle be purely numerical, it may also signal a qualitative transition in the underlying dynamical regime. In the first part of this section, we therefore analyze in detail the mechanism leading to the breakdown of the evolution. In the second part, we characterize the general space-time behavior of the system in the regimes where the simulations remain well controlled.

All numerical simulations are performed on a radial domain $r \in [0, 100]\tilde{M}$. Unless otherwise specified, the coefficient of the Kreiss-Oliger dissipation operator in Eq. (21) is fixed to $\eta_{\text{KO}} = 0.1$.

A. Threshold of numerical breakdown

To determine whether the numerical breakdown observed at large amplitudes A reflects a genuine change in the dynamical behavior of the system or merely a numerical artifact, we investigate the threshold amplitude A_{break} at which the evolution ceases to be well resolved. In particular, we study the dependence of A_{break} on the grid spacing, the time step, and the Kreiss-Oliger dissipation coefficient η_{KO} .

The example in Fig. 5 shows how the evolution of the field leads to a numerical breakdown depending on the choice of the numerical parameter CFL at fixed physical parameters.

The underlying rationale of our investigation is the following: if A_{break} converges toward a stable value under grid refinement and variations of numerical parameters, the breakdown can be attributed to a physical mechanism intrinsic to the dynamics. Conversely, a strong sensitivity of A_{break} to resolution or dissipation would indicate that the observed behavior is primarily of numerical origin.

For each choice of numerical parameters, the critical threshold A_{break} is determined through a bisection procedure, iterated until a target accuracy $\varepsilon_A = 10^{-4}$ is reached. We begin by considering Gaussian initial data with $\sigma = \tilde{M}$ and $r_0 = 10\tilde{M}$, fixing the CFL factor to 0.5 and varying the spatial resolution.

The dependence of A_{break} on the number of grid points N_p is shown in Fig. 6. The data exhibit a monotonic convergence toward a continuum limit as the resolution increases. To estimate the asymptotic value, we employ Richardson extrapolation [43], assuming the nomi-

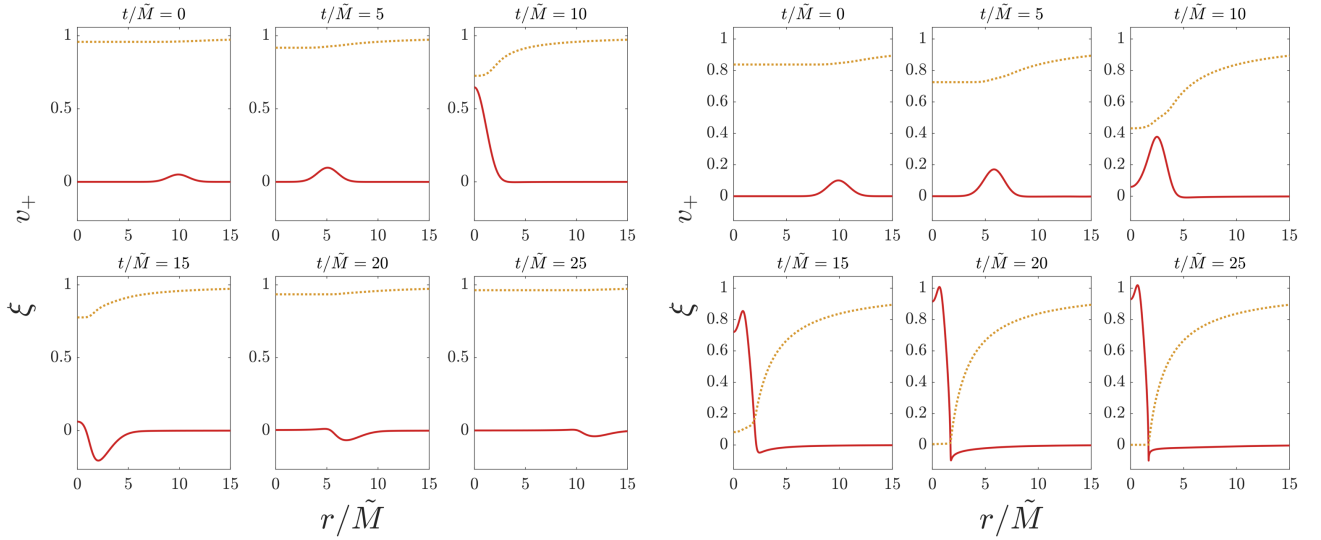


Figure 3. Nonlinear evolution of a standard scalar field (red solid curve) and of the outgoing characteristic velocity v_+ (yellow dashed curve) for a Gaussian initial profile with $\sigma = \tilde{M}$, $r_0 = 10\tilde{M}$. Each small panel corresponds to a different time snapshot. Left panels: Initial amplitude $A = 0.2\tilde{M}$; the field disperses and no horizon forms. Right panels: Initial amplitude $A = \tilde{M}$; the vanishing of v_+ within a finite region signals the formation of a trapped surface and an apparent horizon.

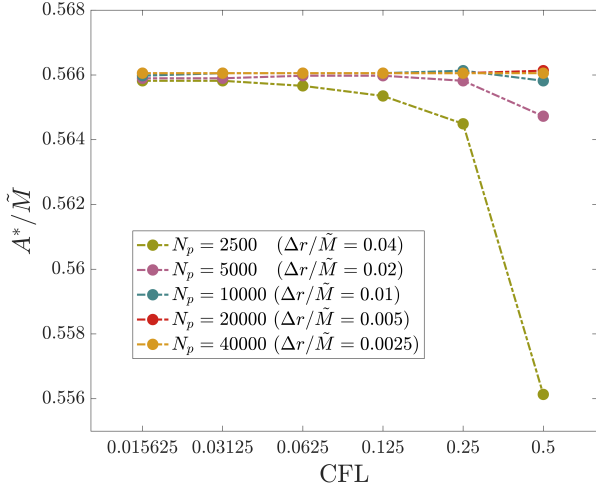


Figure 4. Critical amplitude A^* separating dispersion from black-hole formation as a function of spatial resolution N_p . Different colors denote different CFL factors. As the resolution increases, A^* converges toward $0.566\tilde{M}$, demonstrating numerical robustness.

nal fourth-order convergence ($p = 4$) associated with our centered finite-difference stencils. The value we obtain from the pair of simulations with highest resolution is $A_{\text{break}}^{\text{Rich, fine}} = 1.429\tilde{M}$. We estimate the error associated to the estimate as the difference of this value with the one obtained by extrapolating from the next pair of simulation with highest resolution, namely $N_p = 80000$ and $N_p = 40000$, and we get $\Delta A_{\text{break}}^{\text{Rich}} = 0.006\tilde{M}$. Note that

here we are adopting a conservative approach, as with this procedure we get an estimate of the error on the value obtained from the pair of simulations with lower resolution.

Next, we repeat the same analysis for different choices of the CFL factor. If the observed breakdown were associated with a genuine physical mechanism, one would expect the curves $A_{\text{break}}(N_p)$ obtained at different CFL values to approach a common limit as $\text{CFL} \rightarrow 0$, i.e. as the time step Δt becomes increasingly small relative to the spatial step Δr . Our results, however, display a different trend. At fixed spatial resolution, the critical amplitude A_{break} systematically increases as the CFL factor is reduced. In other words, decreasing the time step while keeping Δr fixed shifts the threshold for breakdown toward larger values of A . This behavior is illustrated in Fig. 7, where different colors correspond to different choices of the CFL factor.

For each fixed CFL value, the convergence pattern with increasing spatial resolution is analogous to that shown in Fig. 6: the sequence $A_{\text{break}}(N_p)$ exhibits monotonic convergence toward an asymptotic value. We estimate this continuum limit using Richardson extrapolation and summarize the extrapolated values, together with their associated uncertainties, in Table I.

The absence of a common asymptotic value toward which A_{break} converges indicates that the observed breakdown is a numerical artifact rather than a genuine physical effect. In particular, the strong dependence of A_{break} on the CFL factor shows that the choice of time step plays a dominant role in resolving the dynamics. In other words, our results suggest that a regular evolution can, in principle, always be achieved provided the CFL factor is sufficiently small.

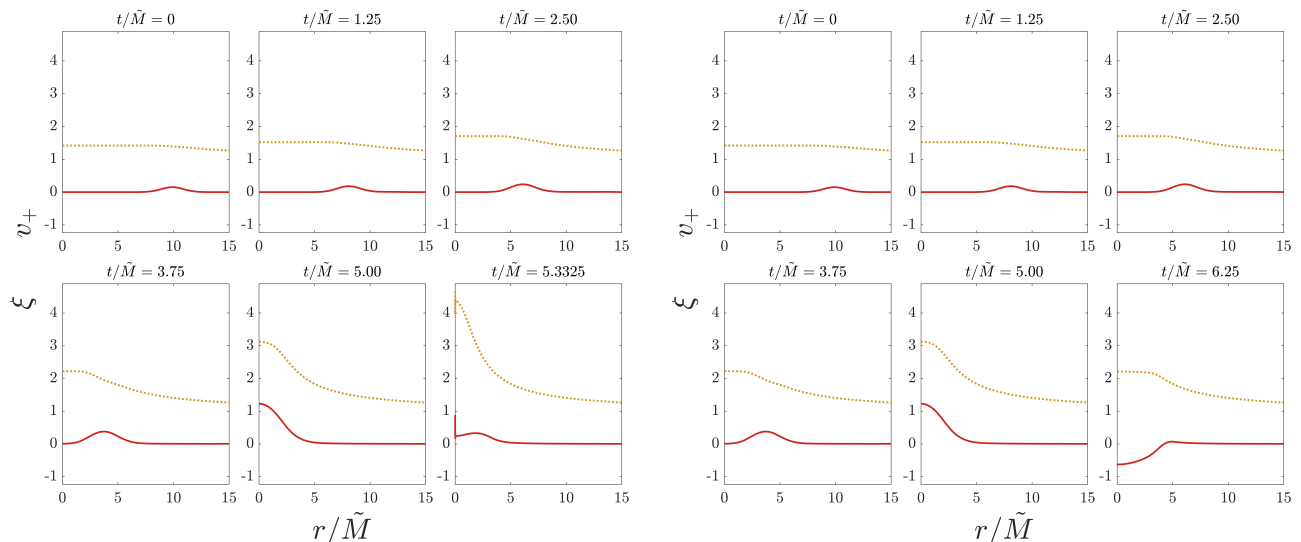


Figure 5. Nonlinear evolution of a phantom scalar field ξ (red solid curve) and of the outgoing characteristic velocity v_+ (yellow dashed curve) for Gaussian initial data with $\sigma = \tilde{M}$ and $r_0 = 10\tilde{M}$. Each small panel shows a different time snapshot of the evolution. Left panels: initial amplitude $A = 1.5\tilde{M}$ with CFL = 0.5. The evolution develops irregular features at the origin and eventually breaks down. Right panels: same initial data but with CFL = 0.25, while the spatial resolution Δr and the Kreiss-Oliger dissipation coefficient η_{KO} are kept fixed. In this case the evolution remains well behaved throughout the simulation (note that the times shown in the bottom-right panels differ from those in the corresponding panels on the left).

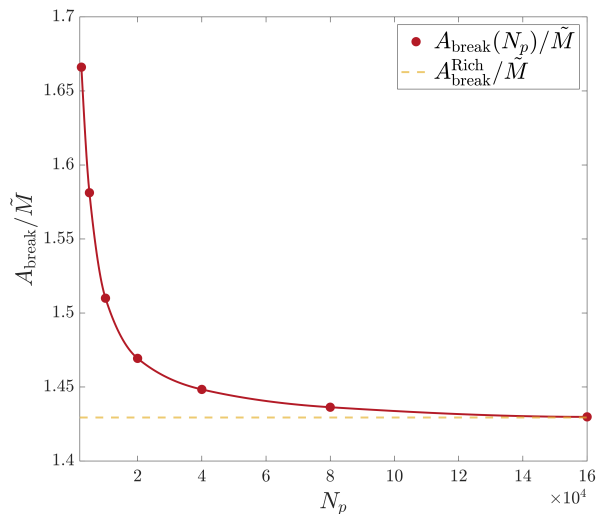


Figure 6. Breakdown threshold for the amplitude of a Gaussian wave packet with $\sigma = \tilde{M}$ and $r_0 = 10\tilde{M}$, estimated via bisection and shown as a function of the radial resolution N_p . Red dots denote the values of $A_{\text{break}}(N_p)$ extracted from the numerical simulations, while the dashed line is the extrapolated value for large N_p .

In all simulations performed with the *phantom* field, the Misner-Sharp mass remains consistently negative throughout the evolution. This behavior is consistent with the repulsive character of the field's energy-momentum tensor, which violates the standard energy

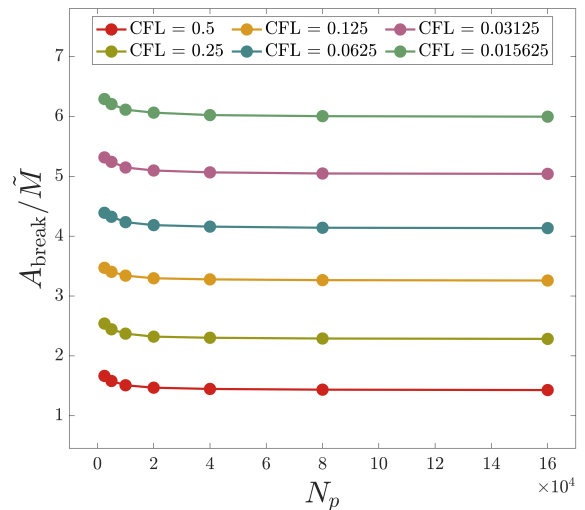


Figure 7. Critical threshold A_{break} as a function of the number of radial grid points N_p for different values of the CFL factor. The curves do not converge toward a common continuum limit; instead, A_{break} systematically increases as the CFL factor is reduced. This behavior indicates that the observed breakdown is of numerical origin and that the resolution of the dynamics is primarily controlled by the choice of time step.

conditions, including in particular the null and strong energy conditions.

Figure 8 shows the absolute value $|M_{\text{MS}}|$ at the critical

Table I. Extrapolated critical amplitude $A_{\text{break}}^{\text{Rich}}$ as a function of the CFL, obtained through Richardson extrapolation.

CFL	$A_{\text{break}}^{\text{Rich}}$	$\Delta A_{\text{break}}^{\text{Rich}}$
0.5	1.429	0.006
0.25	2.284	0.006
0.125	3.259	0.006
0.0625	4.134	0.005
0.03125	5.040	0.005
0.015625	5.995	0.008

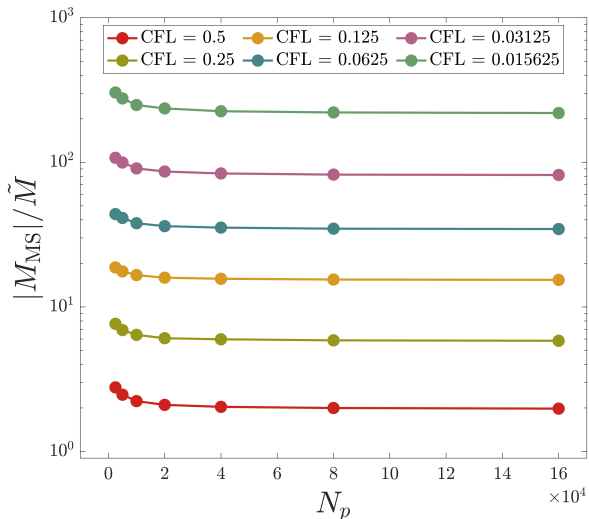


Figure 8. Absolute value of the Misner-Sharp mass, $|M_{\text{MS}}|$, computed at the critical amplitude A_{break} as a function of the number of radial grid points N_p , for different values of the CFL factor.

amplitude A_{break} displayed in Fig. 7, plotted as a function of the spatial resolution and the CFL factor.

Even for absolute values of the Misner-Sharp mass as large as $|M_{\text{MS}}| \approx 200\tilde{M}$, obtained in runs with larger CFL factors, the evolution remains regular. For comparison, in the case of a canonical scalar field such a mass would correspond to a black hole with areal radius $r_{\text{H}} = 2M \approx 400\tilde{M}$. In the present case, however, no trapped region forms and the field ultimately disperses.

Overall, within the explored parameter range, our results show no evidence for the formation of trapped surfaces, naked singularities, or alternative exotic configurations during the collapse of the phantom field.

Furthermore, to verify that the observed breakdown is primarily driven by the choice of time step rather than by the Kreiss-Oliger dissipation operator, we performed an additional analysis varying the dissipation parameter η_{KO} , with fixed $r_0 = 10\tilde{M}$ and $\sigma = \tilde{M}$. The results are summarized in Table II, where different columns report the values of A_{break} obtained for various choices of the CFL factor and spatial resolution. We find that the critical amplitude depends only weakly on η_{KO} , with varia-

Table II. Critical amplitude A_{break} as a function of the dissipation parameter η_{KO} , computed at different spatial resolutions and CFL factors.

η_{KO}	$\frac{A_{\text{break}}}{\tilde{M}}$	CFL = 0.5	CFL = 0.0625	CFL = 0.015625
	$N_p = 40000$	$N_p = 80000$	$N_p = 160000$	
0.025	1.442	4.138	5.989	
0.05	1.446	4.139	5.992	
0.1	1.448	4.143	5.996	
0.2	1.453	4.150	6.003	
0.4	1.466	4.163	6.019	

tions of at most a few $\times 10^{-2}$, whereas it is significantly more sensitive to the numerical resolution and the time step. This demonstrates that our determination of the critical threshold is robust with respect to the amount of numerical dissipation and confirms that the dominant source of the breakdown is the temporal discretization.

To gain further insight into the system's dynamics, we now investigate how the physical parameters of the initial data affect the threshold for breakdown. In particular, we fix the center of the wave packet at $r_0 = 20\tilde{M}$ and consider different values of the width parameter σ . In this additional set of simulations we adopt $N_p = 80000$, which yields estimates of the critical amplitude close to the asymptotic value at fixed CFL (cf. Fig. 7). The results are summarized in Fig. 9, where we plot the critical amplitude A_{break} as a function of σ for several choices of the CFL factor.

We observe that A_{break} increases monotonically with the width of the wave packet. This trend can be qualitatively understood from the structure of the stress-energy tensor: the effective energy and momentum densities depend on derivatives of ξ . A broader wave packet has smaller spatial gradients, which reduce the magnitude of these derivative terms. Consequently, a larger amplitude is required to produce comparable curvature effects and approach the regime where the evolution becomes numerically problematic.

However, the separation between the curves corresponding to different CFL values indicates the absence of convergence. As the time step is reduced, the threshold shifts toward progressively larger amplitudes, with no sign of saturation. This behavior is consistent with our previous analyses and reinforces the conclusion that no physically meaningful, convergent value of A_{break} exists, and that the breakdown is driven by numerical rather than dynamical effects.

Finally, we repeat the analysis using the phantom-field profile defined in Eq. (23). For all simulations with the tanh wave packet, the parameters \hat{r}_1 , \hat{r}_2 , and σ are set to $\hat{r}_1 = 10\tilde{M}$, $\hat{r}_2 = 30\tilde{M}$ and $\sigma = \tilde{M}$, respectively, which preserve the validity of the boundary conditions of the domain. This additional set of simulations allows us to test the robustness of the observed behavior and to assess whether the spatial distribution of the energy influences

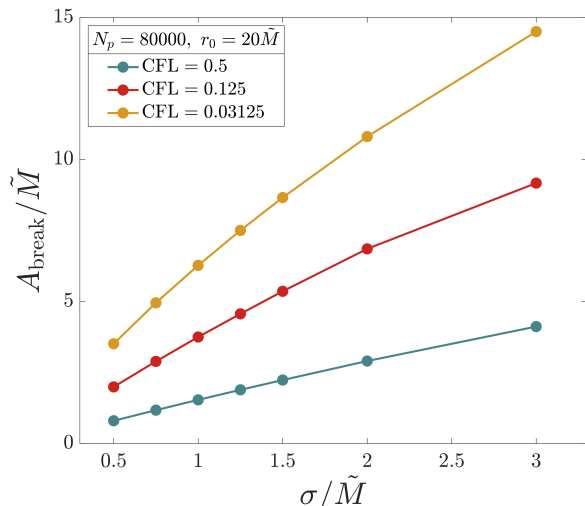


Figure 9. Critical threshold A_{break} as a function of the width σ , for different values of the CFL. The simulations are performed with $N_p = 80000$ and $r_0 = 20\tilde{M}$.

the results. From a physical standpoint, the two initial configurations correspond to qualitatively different perturbations. The Gaussian packet represents a localized and smooth excitation with narrow-band spectral content: its energy is concentrated around a dominant frequency, and the collapse proceeds in a relatively simple and temporally coherent manner. By contrast, the double-tanh profile describes an extended configuration featuring quasi-stationary regions separated by steep gradients at the edges. These sharp transitions introduce higher-frequency components and a slower spectral decay, resulting in a broader distribution of scales.

In dynamical terms, this distinction translates into a more intricate time evolution. While the Gaussian perturbation typically propagates inward and either disperses or collapses within a finite time, the step-like configuration evolves more gradually, producing successive wavefronts and a less regular temporal pattern. This setup therefore provides a complementary probe of the dynamics, allowing us to assess how sharper gradients and multiple time scales affect the gravitational focusing properties of the phantom field.

In Fig. 10 we summarize the results obtained with the double-tanh initial profile. The upper panel shows the critical amplitude A_{break} , while the lower panel displays the absolute value of the Misner-Sharp mass at the onset of the breakdown, for different spatial resolutions and CFL factors. The qualitative behavior is fully consistent with that found for the Gaussian profile. In particular, we observe clear convergence of the critical threshold A_{break} with increasing spatial resolution, whereas no analogous convergence emerges with respect to the CFL factor.

This further supports the conclusion that the observed breakdown is a numerical artifact and that it is predom-

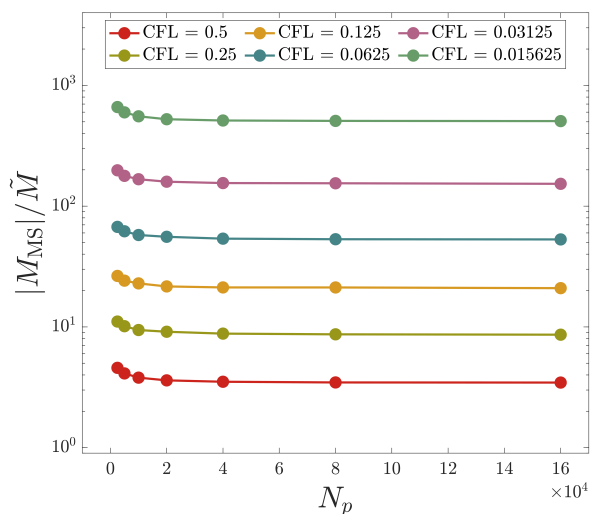
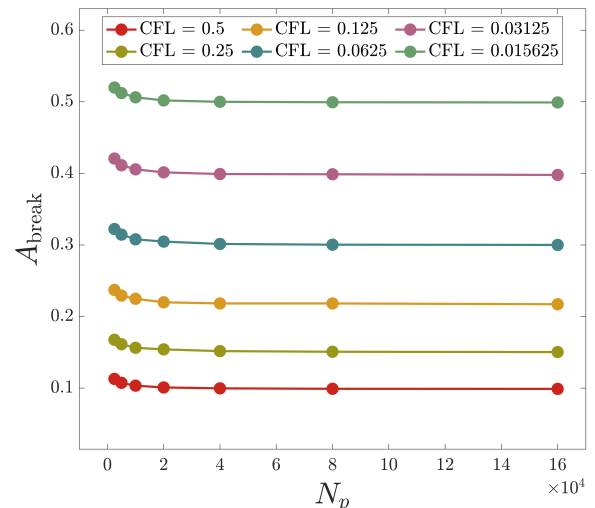


Figure 10. Threshold of numerical breakdown as a function of the number of grid points, for different choices of the CFL factor, in the case of an initial phantom wave packet of tanh-type profile, Eq. (23). The upper panel shows the values of the critical amplitude A_{break} , and the lower panel the corresponding Misner-Sharp mass of the system (in absolute value). Both quantities show no clear convergence trend as the CFL decreases, confirming that the numerical breakdown is dominated by the choice of the time step, rather than by spatial resolution.

inantly controlled by the choice of time step rather than by the physical properties of the initial configuration.

B. Spacetime behavior of the curvature

To better understand the origin of the observed breakdown, we analyze the spacetime evolution of the Kretschmann scalar for representative configurations. We consider Gaussian initial data with $r_0 = 10\tilde{M}$ and

$\sigma = \tilde{M}$, using $N_p = 20000$ grid points.

We first examine a simulation with moderate amplitude, $A = 0.5\tilde{M}$, and $\text{CFL} = 0.0625$. The left panel of Fig. 11 displays the Kretschmann scalar $K(t, r)$ over the full computational domain ($r \in [0, 100]\tilde{M}$, $t \in [0, 30]\tilde{M}$), while the right panel shows a zoom into the central region ($r \in [0, 12]\tilde{M}$, $t \in [0, 20]\tilde{M}$). The wave packet propagates inward from $r \approx 10\tilde{M}$ and reaches the center at $t \approx 8\tilde{M}$. Around $t \approx 8\tilde{M} - 10\tilde{M}$ the curvature exhibits a transient peak, after which the phantom field disperses outward. In the outer regions, where the scalar amplitude becomes negligible, the geometry asymptotically approaches flat spacetime, albeit modified by the negative effective mass of the configuration. Throughout the evolution the curvature remains finite, and no trapped surfaces form.

Increasing the amplitude to $A = 3.0\tilde{M}$ (still with $\text{CFL} = 0.0625$) leads to qualitatively similar dynamics, shown in Fig. 12 for the central region ($r \in [0, 12]\tilde{M}$, $t \in [0, 6]\tilde{M}$). The curvature structure becomes more intricate, featuring oblique ridges corresponding to regions of enhanced curvature. The main bright band represents the outgoing front generated after the initial compression phase, while subsequent weaker structures correspond to rarefaction tails and partial reflections. The peak curvature reaches $K \sim 10^2\tilde{M}^{-4}$, about two orders of magnitude larger than in the $A = 0.5\tilde{M}$ case, yet remains finite. No indication of horizon formation or curvature divergence is observed.

Physically, this behavior reflects the repulsive character of the phantom field: the negative kinetic term introduces an effective negative energy density that counteracts the initial focusing. The curvature grows rapidly during the initial compression, reaches a maximum, and is then followed by reflection and dispersion rather than collapse.

Interestingly, the process now occurs on a much shorter timescale, around $t \simeq 2\tilde{M}$, due to the fact that the larger (negative) effective mass of the phantom field induces larger modifications on metric functions and causes the coordinate characteristic speeds to increase. Such effect is shown in Fig. 13, where we plot the evolution of the absolute value of the characteristic velocities, v_{char} , extracted at the innermost physical grid point, for the simulations with $A = 0.5\tilde{M}$, $A = 3.0\tilde{M}$ and $A = 5.0\tilde{M}$ (to be discussed below). As we can see, the characteristic speeds grow during the evolution and depend significantly on the initial amplitude, changing by orders of magnitude. Overall v_{char} grows with A , causing the dynamics to be faster.

This effect also clarifies the origin of the numerical breakdown and the observed dependence of the critical threshold on the CFL factor. We operationally defined the CFL factor as in Eq. (18), $\text{CFL} = \Delta t / \Delta r$, which corresponds to the actual definition (17) only when $v_{\text{char}} = 1$. However, since for large values of A the characteristic speeds increase substantially, the original CFL factor in Eq. (17), $\overline{\text{CFL}} = v_{\text{char}} \text{CFL}$, can exceed the upper bound for stability and lead the numerical evolution

to a breakdown. For a given initial amplitude, decreasing CFL also reduces $\overline{\text{CFL}}$ and can restore stability, postponing the breakdown to larger values of the amplitude and the characteristic velocity.

Lastly, we study the case of a very large initial amplitude, $A = 5\tilde{M}$, for which nonlinear effects become even more pronounced. In this regime the characteristic speeds increase dramatically (see Fig. 13), and the chosen time step is no longer small enough to ensure stability. Indeed, a simulation performed with $\text{CFL} = 0.0625$ exhibits a rapid growth of the Kretschmann scalar up to $K \sim 10^{11}\tilde{M}^{-4}$, signaling numerical breakdown, as shown in the left panel of Fig. 14 and also by the purple dashed curve in Fig. 13.

Reducing the CFL factor to 0.015625 restores a regular evolution, as shown in the right panel of Fig. 14 (see also the green curve in Fig. 13). The wave packet now reaches the origin very early ($t \simeq 0.5\tilde{M}$), followed by a bounce and rarefaction phase that generates multiple outgoing curvature pulses.

A closer inspection reveals that the repulsive contribution of the negative energy density becomes dominant almost immediately: part of the wave packet is prevented from reaching the center and propagates outward instead. The curvature remains finite ($K \lesssim 10^3\tilde{M}^{-4}$) and gradually decays over time. No trapped surfaces, singularities, or other exotic configurations are observed.

V. CONCLUSIONS

In this work we have investigated the nonlinear gravitational collapse of a phantom scalar field in asymptotically flat spacetime. Because the kinetic term of the phantom field enters the action with the opposite sign relative to a canonical scalar field, its energy density can become negative. This raises the possibility that gravitational collapse could lead to exotic outcomes, such as negative-mass configurations, naked singularities, or other violations of the cosmic censorship conjecture.

To address this *gedanken experiment*, we performed high-accuracy numerical-relativity simulations of spherically symmetric configurations, evolving smooth and regular wave packets of the phantom scalar field across a wide range of amplitudes. The numerical scheme was validated through convergence tests and monitoring of the constraint equations.

Our results show that none of the initial data considered lead to the formation of trapped surfaces or singular end states. Instead, the scalar field disperses and the spacetime relaxes toward a regular asymptotically flat geometry. In particular, we find no evidence for the formation of negative-mass Schwarzschild solutions or other stationary exotic remnants. Within the parameter space explored here, the nonlinear dynamics therefore appears to prevent the realization of configurations that would violate cosmic censorship.

All simulations were performed by solving the

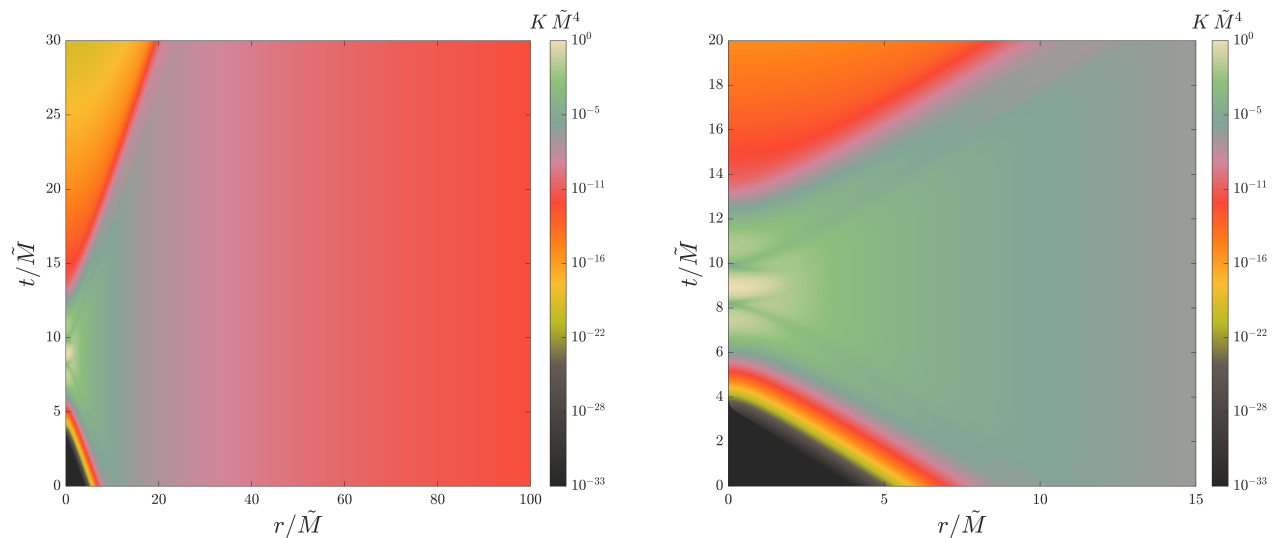


Figure 11. Spacetime evolution of the Kretschmann scalar $K(t, r)$ for a Gaussian phantom wave packet with $A = 0.5\tilde{M}$, $\sigma = \tilde{M}$, and $r_0 = 10\tilde{M}$. The left panel shows the full domain, while the right panel zooms into the central packet region.

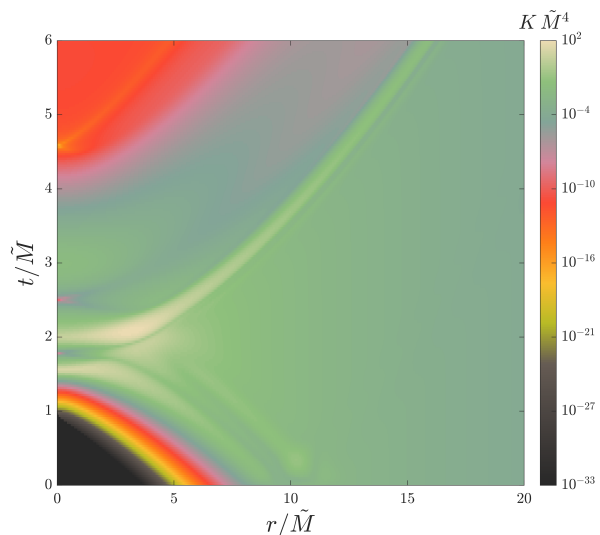


Figure 12. Spacetime evolution of the Kretschmann scalar $K(t, r)$ for a Gaussian phantom wave packet with amplitude $A = 3.0\tilde{M}$.

Einstein-Klein-Gordon system in spherical symmetry, discretized using the method of lines and evolved with a fourth-order Runge-Kutta integrator. We considered two classes of initial data, a Gaussian pulse and a double-tanh profile, adopting a Choptuik-like strategy in which the shape and width were fixed while the amplitude was varied. In both families, increasing the temporal resolution removes the apparent numerical breakdown: rather than collapsing, the scalar field ultimately disperses.

The breakdown observed at large amplitudes is therefore purely numerical. It arises when strong metric gradients cause the local characteristic speeds to grow signif-

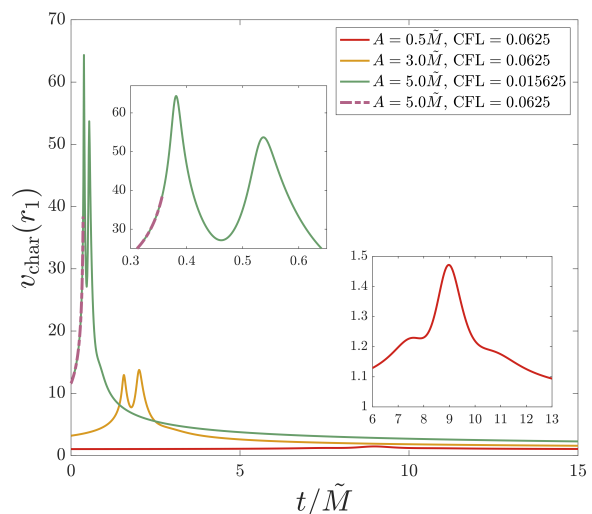


Figure 13. Time evolution of the absolute value of the characteristic velocity, $v_{\text{char}}(r_1)$, evaluated at the innermost physical grid point, for Gaussian wave packets with width $\sigma = \tilde{M}$ and center $r_0 = 10\tilde{M}$. The curves correspond to different amplitudes of the scalar field. The red, yellow and purple curves denote simulations with Courant factor $\text{CFL} = 0.0625$, while the green curve corresponds to a smaller value $\text{CFL} = 0.015625$ for the simulation with the largest amplitude. The insets show zoomed views of the highlighted region for the low-amplitude case $A = 0.5\tilde{M}$, and for the high-amplitude case, $A = 5.0\tilde{M}$.

icantly. Under these conditions the Courant–Friedrichs–Lewy stability criterion is violated, triggering numerical instabilities. Reducing the CFL factor restores stable and regular evolution.

We further analyzed the nonlinear dynamics through the evolution of the Kretschmann scalar, which pro-

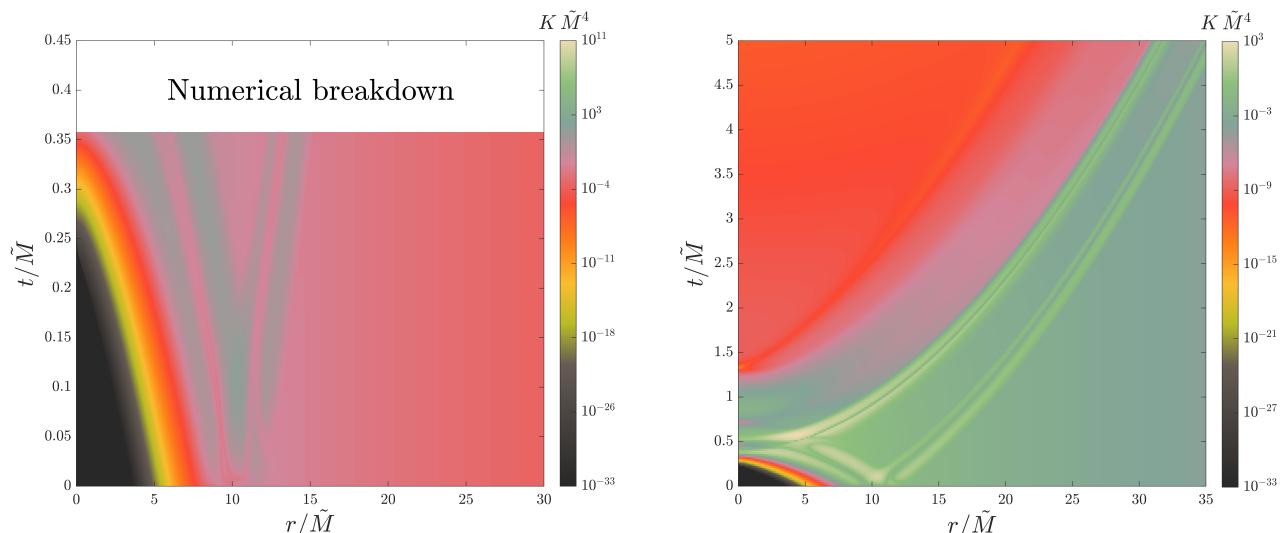


Figure 14. Left: Spacetime evolution of the Kretschmann scalar $K(t, r)$ for a Gaussian phantom wave packet with $A = 5\tilde{M}$ and CFL = 0.0625. The evolution undergoes numerical breakdown. Right: Same configuration as in the left panel, but with CFL = 0.015625. The evolution remains regular.

vides a clear diagnostic of curvature amplification, wave focusing, and subsequent dispersion. Even for configurations corresponding to effective masses as negative as $M_{\text{MS}} \sim -200\tilde{M}$, the curvature remains finite and no trapped surfaces form. For comparison, a canonical scalar field with similar parameters would produce black holes with macroscopic horizons.

Within the parameter space explored here, we find no indication of singularity formation, horizon development, or alternative stationary solutions such as wormhole-like geometries. Instead, the repulsive character of the phantom field systematically counteracts gravitational focusing and drives the system toward a regular dispersive state, consistently with the behavior reported in Refs. [35, 36].

The numerical framework developed in this work proves robust and well controlled, successfully handling the highly dynamical regime associated with large characteristic velocities. Although the simulations require fine spatial and temporal resolution, their convergence properties and stability behavior are well understood.

Overall, our results indicate that cosmic censorship appears to remain dynamically preserved even in the presence of negative-energy matter.

ACKNOWLEDGMENTS

This research was supported by the MUR FIS2 Advanced Grant ET-NOW (CUP: B53C25001080001) and by the INFN TEONGRAV initiative. Numerical computations have been performed at the Vera and CHRONOS clusters supported by the Italian Ministry of Research and by Sapienza University of Rome.

Appendix A: Code validation

To quantify the accuracy of the nonlinear 1 + 1 code, we check how the violation of the radial constraint for β (Eq. (12)) scales with resolution. Such constraint violation (CV) is evaluated as

$$CV_{\beta}(t, r) = \partial_r \beta + \frac{e^{2\beta}(Cr^2\Pi^2 + 1) + Cr^2\Theta^2 - 1}{2r}, \quad (\text{A1})$$

where $\partial_r \beta$ is computed numerically.

Since both spatial discretization and time integration are implemented with fourth-order schemes, halving the spatial grid spacing is expected to reduce the constraint violation according to the relation

$$CV_{\Delta r_{\text{coarse}}} = \left(\frac{\Delta r_{\text{coarse}}}{\Delta r_{\text{fine}}}\right)^4 CV_{\Delta r_{\text{fine}}} = 16 CV_{\Delta r_{\text{fine}}}, \quad (\text{A2})$$

where $\Delta r_{\text{coarse}} = 2\Delta r_{\text{fine}}$. Therefore, if the implementation is correct, the fine-grid CV multiplied by 16 should overlap with the coarse-grid CV.

We perform convergence tests using pairs of simulations with spatial resolutions differing by a factor two (e.g., $\Delta r_{\text{coarse}} = 0.01\tilde{M}$, $\Delta r_{\text{fine}} = 0.005\tilde{M}$). Each pair is evolved with various CFL values to separately assess the effects of spatial and temporal resolution.

First we consider the case of an initial Gaussian wave packet with $A = \tilde{M}$, $\sigma = \tilde{M}$ and $r_0 = 10\tilde{M}$. Figure 15 shows the scaling of CV_{β} at $t = 30\tilde{M}$ for CFL = 0.5. After rescaling the fine-grid curve by 16, we observe excellent overlap across the entire domain, demonstrating global fourth-order convergence. The inset highlights the region $25 < r/\tilde{M} < 32$, where the scalar field is localized and the violations are largest, yet still obey the expected scaling.

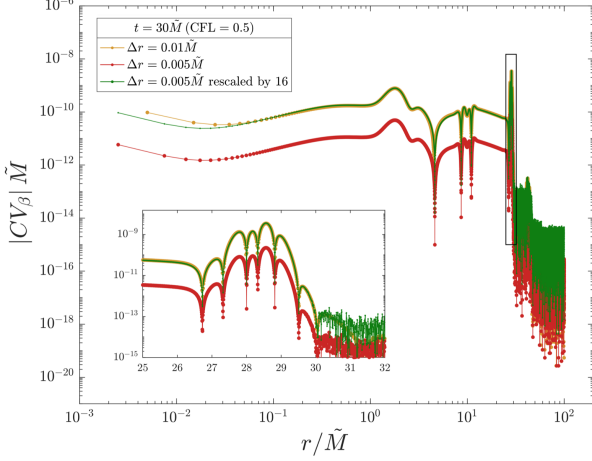


Figure 15. Fourth-order scaling of the constraint violation CV_β at $t = 30\tilde{M}$, with initial data $(A, \sigma, r_0) = (1.0, 1.0, 10)\tilde{M}$ and CFL = 0.5. Yellow: $\Delta r = 0.01\tilde{M}$; red: $\Delta r = 0.005\tilde{M}$; green: fine grid data rescaled by 16.

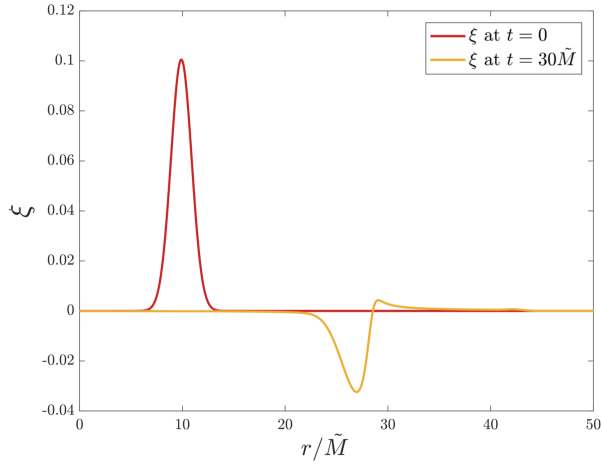


Figure 16. Radial profile of ξ for $\Delta r = 0.05\tilde{M}$, $(A, \sigma, r_0) = (1.0, 1.0, 10)\tilde{M}$, and CFL = 0.5. Red: initial data; yellow: profile at $t = 30\tilde{M}$.

To correlate constraint violation with field dynamics, Fig. 16 shows the radial profile of ξ at $t = 0$ and $t = 30\tilde{M}$. The largest violations occur precisely where the field amplitude is significant, as expected since the constraint contains matter terms.

Next, we repeat the analysis for smaller CFL values. Figure 17 shows CV_β at $t = 30\tilde{M}$ for CFL = 0.0625. Fourth-order convergence is again observed across most of the domain when rescaling by 16. In localized regions, improved overlap is obtained with a factor 32. This behavior is attributable to the fifth-order Kreiss-Oliger dissipation term (21), which modifies the highest-frequency components and slightly alters the effective convergence order in smooth regions.

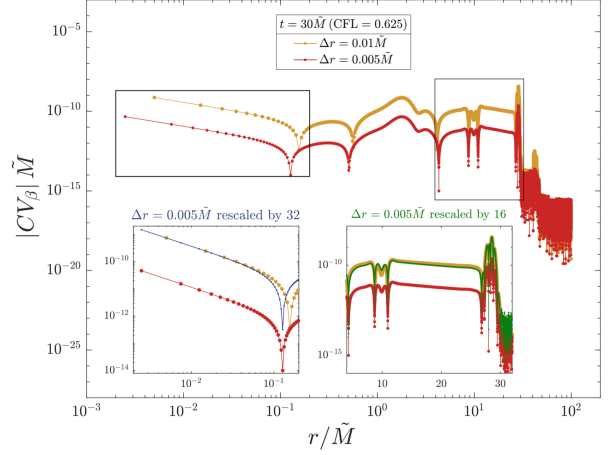


Figure 17. Constraint violation CV_β at $t = 30\tilde{M}$ for CFL = 0.0625. Yellow: $\Delta r = 0.01\tilde{M}$; red: $\Delta r = 0.005\tilde{M}$.

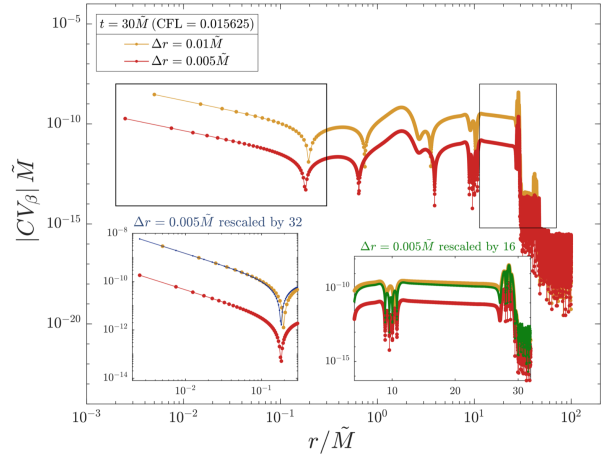


Figure 18. Constraint violation CV_β at $t = 30\tilde{M}$ for CFL = 0.015625.

A similar behavior is observed for CFL = 0.015625, as shown in Fig. 18. At late times ($t = 30\tilde{M}$), mild deviations from ideal fourth-order scaling appear more prominently. Such deviations are consistent with an increased relative influence of the dissipation term once the field amplitude has decreased and the solution becomes smoother.

To corroborate this hypothesis, we examined earlier times when nonlinear dynamics are stronger and the dissipative term is subdominant. At $t = 7.5\tilde{M}$, shortly before the collapse phase, fourth-order scaling is clearly recovered even for CFL = 0.015625, as shown in Fig. 19.

Overall, these tests demonstrate that the numerical implementation achieves the expected fourth-order convergence and that deviations at late times are consistent with the influence of Kreiss-Oliger dissipation rather than with deficiencies in the underlying scheme.

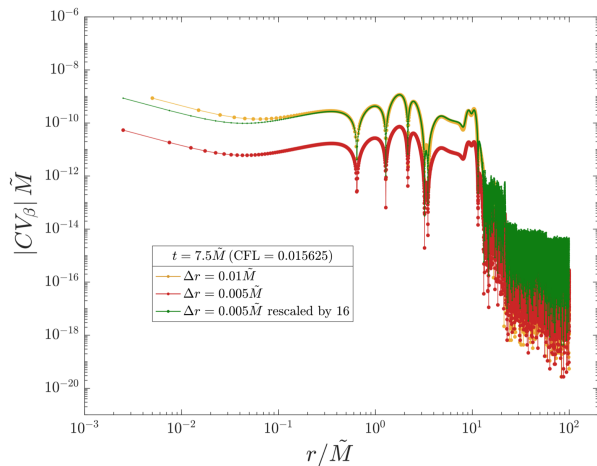


Figure 19. Constraint violation CV_β at $t = 7.5\tilde{M}$ for $CFL = 0.015625$.

-
- [1] R. P. Geroch, *Annals Phys.* **48**, 526 (1968).
- [2] R. C. Henry, *Astrophys. J.* **535**, 350 (2000), arXiv:astro-ph/9912320.
- [3] C. W. Misner, *J. Math. Phys.* **4**, 924 (1963).
- [4] R. M. Wald, *General Relativity* (Chicago Univ. Pr., Chicago, USA, 1984).
- [5] S. Hawking, *Proc. Roy. Soc. Lond. A* **294**, 511 (1966).
- [6] S. W. Hawking and G. F. R. Ellis, *The Large Scale Structure of Space-Time*, Cambridge Monographs on Mathematical Physics (Cambridge University Press, 2023).
- [7] R. Steinbauer, *Jahresbericht der Deutschen Mathematiker-Vereinigung* **125**, 73–119 (2023).
- [8] K. Landsman, *Foundations of Physics* **51**, 42 (2021).
- [9] R. Penrose, *Phys. Rev. Lett.* **14**, 57 (1965).
- [10] R. Penrose, *Annals N. Y. Acad. Sci.* **224**, 125 (1973).
- [11] D. Christodoulou, *Annals Math.* **140**, 607 (1994).
- [12] T. Harada, *Pramana* **63**, 741 (2004), arXiv:gr-qc/0407109.
- [13] A. Ori and T. Piran, *Phys. Rev. Lett.* **59**, 2137 (1987).
- [14] J. M. Martin-Garcia and C. Gundlach, *Phys. Rev. D* **68**, 024011 (2003), arXiv:gr-qc/0304070.
- [15] P. S. Joshi and I. H. Dwivedi, *Phys. Rev. D* **47**, 5357 (1993), arXiv:gr-qc/9303037.
- [16] R. Penrose, *Riv. Nuovo Cim.* **1**, 252 (1969).
- [17] R. Penrose, *J. Astrophys. Astron.* **20**, 233 (1999).
- [18] D. Christodoulou, *Annals Math.* **149**, 183 (1999), arXiv:math/9901147.
- [19] V. E. Hubeny, *Phys. Rev. D* **59**, 064013 (1999), arXiv:gr-qc/9808043.
- [20] I. Semiz, *Gen. Rel. Grav.* **43**, 833 (2011), arXiv:gr-qc/0508011.
- [21] L. Lehner and F. Pretorius, *Phys. Rev. Lett.* **105**, 101102 (2010), arXiv:1006.5960 [hep-th].
- [22] P. Figueras, T. Franca, C. Gu, and T. Andrade, *Phys. Rev. D* **107**, 044028 (2023), arXiv:2210.13501 [hep-th].
- [23] R. Wald, *Annals of Physics* **82**, 548 (1974).
- [24] T. Jacobson and T. P. Sotiriou, *J. Phys. Conf. Ser.* **222**, 012041 (2010), arXiv:1006.1764 [gr-qc].
- [25] E. Barausse, V. Cardoso, and G. Khanna, *Phys. Rev. Lett.* **105**, 261102 (2010), arXiv:1008.5159 [gr-qc].
- [26] M. Colleoni and L. Barack, *Phys. Rev. D* **91**, 104024 (2015), arXiv:1501.07330 [gr-qc].
- [27] D. Christodoulou, in *12th Marcel Grossmann Meeting on General Relativity* (2008) pp. 24–34, arXiv:0805.3880 [gr-qc].
- [28] T. W. Baumgarte and S. L. Shapiro, *Numerical Relativity: Solving Einstein's Equations on the Computer* (Cambridge University Press, 2010).
- [29] M. W. Choptuik, *Phys. Rev. Lett.* **70**, 9 (1993).
- [30] P. R. Brady, C. M. Chambers, and S. M. C. V. Goncalves, *Phys. Rev. D* **56**, R6057 (1997), arXiv:gr-qc/9709014.
- [31] M. W. Choptuik, E. W. Hirschmann, S. L. Liebling, and F. Pretorius, *Phys. Rev. Lett.* **93**, 131101 (2004), arXiv:gr-qc/0405101.
- [32] S. Hod and T. Piran, *Phys. Rev. D* **55**, 3485 (1997), arXiv:gr-qc/9606093.
- [33] C. Gundlach, *Adv. Theor. Math. Phys.* **2**, 1 (1998), arXiv:gr-qc/9712084.
- [34] C. R. Evans and J. S. Coleman, *Phys. Rev. Lett.* **72**, 1782 (1994), arXiv:gr-qc/9402041.
- [35] A. Nakonieczna, M. Rogatko, and R. Moderski, *Phys. Rev. D* **86**, 044043 (2012), arXiv:1209.1203 [hep-th].
- [36] A. Nakonieczna and M. Rogatko, *AIP Conf. Proc.* **1514**, 43 (2013), arXiv:1301.1561 [hep-th].
- [37] K. Atkinson, W. Han, and D. E. Stewart, *Numerical solution of ordinary differential equations* (John Wiley & Sons, 2009).
- [38] J. L. Ripley and F. Pretorius, *Class. Quant. Grav.* **36**, 134001 (2019), arXiv:1903.07543 [gr-qc].
- [39] H.-O. Kreiss (1973).
- [40] M. C. Babiuc *et al.*, *Class. Quant. Grav.* **25**, 125012 (2008), arXiv:0709.3559 [gr-qc].
- [41] G. Abreu and M. Visser, *Phys. Rev. D* **82**, 044027 (2010), arXiv:1004.1456 [gr-qc].
- [42] F. Thaalba, M. Bezares, N. Franchini, and T. P. Sotiriou,

Phys. Rev. D **109**, L041503 (2024), arXiv:2306.01695 [gr-qc].

[43] L. F. Richardson, Philosophical Transactions of the Royal Society of London Series A **210**, 307 (1911).